A local optical probe for measuring motion and stress in a nanoelectromechanical system

A. Reserbat-Plantey, L. Marty, O. Arcizet, N. Bendiab & V. Bouchiat

Institut Néel, CNRS et Université Joseph Fourier, BP 166, F-38042 Grenoble Cedex 9, France-UJF-INP, Grenoble, France
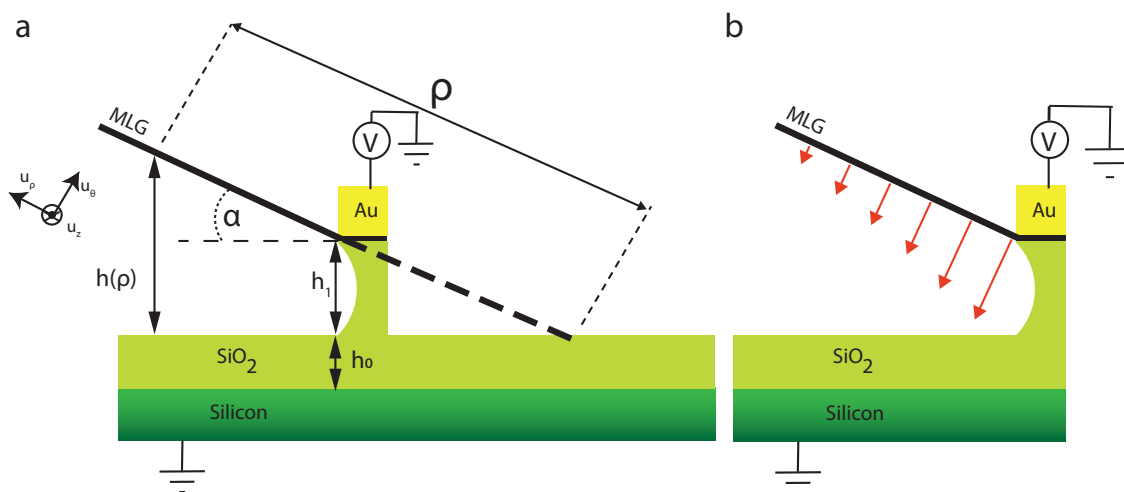
FIGURE S1. *a : Schematic view of the multilayer graphene NEMS device. The cantilever angle α and the cavity length $h(\rho)$ characterize the wedged structure. b : red arrows are qualitative view of the electrostatic force applied along the wedged cantilever.*

I. OPTICAL INTERFERENCES IN A WEDGED CAVITY

The samples studied in the main text consist in a Multi Layer Graphene (MLG) planar cantilevers overhanging oxidized silicon with a wedge angle α. This optical cavity is composed of four optical elements : a bulk silicon backmirror with optical index $n_{Si}(\lambda = 530nm) = 4.151 + 0.029i$, a layer of silicon oxide ($\sim$100 nm) with optical index $n_{SiO_2}(\lambda = 530nm) = 1.544$, a variable thickness of air/vaccum wedge ($n_0 = 1$) and a 30-nm-thick MLG membrane with optical index $n_{MLG} = 2.9 - 0.8i$. MLG optical index is not strongly λ-dependent[1,2]. Equal thickness optical interferences fringes are observed in wedge device. They are called Fizeau fringes[3]. These fringes do not exhibit the high finesse characteristic of Fabry-Perot

fringes because of the non-parallel wedge geometry which causes wave detrapping at higher interference order[4]. As discussed by Brossel[5], interference effects within a wedged cavity can be described by adding to the standard Fabry-Pérot formula a non-linear corrective term in the optical path δ :

$$\delta = 2mh(\rho) - \frac{4}{3}h(\rho)\alpha^2 m^3 \tag{1}$$

If the cubic term induces a shift greater than $\lambda/2$, resulting interferences contrast will degrade rather than sharpen upon increasing the interference order $m = 2h/\lambda$. The maximum detected interference order m is then defined by the visibility criterion, function of the wavelength λ, the wedge thickness $h(\rho)$ and the wedge angle α as :

$$m^3 \leq \frac{3\lambda}{8h(\rho)\alpha^2} \tag{2}$$

Considering the visibility criterion in our case (Eq. 2), m values are less than 10 for typical angles $\alpha \in [5°; 35°]$ since $h(\rho)$ is order of λ.

The interference profile shown in Fig. S2a can be qualitatively understood by using a simplified approach. It consists in only considering a two wave interference effect, corresponding to the reflections on the MLG and Si planes respectively. The results are sketched in Fig. S2b. The protocol consists in varying the focussed spot of an incoming Gaussian beam, and measuring the overlap of the reflected field with the spatial profile of the incoming field, that also match the detection mode. The reflected field is simply estimated by taking the complex sum of the fields reflected by the two planes, and taking into account the field reflection and transmission coefficients on each mirror. Note that no spatially incoherent scattering has been considered in this very simple approach, which explains the absence of the bright features observed experimentally at the plane location. However, the general characteristics of the Fizeau fringes can be reproduced. Note also that in order to obtain a correct fringe pattern, one has to take into account the phase curvature of the fields, as a simple intensity calculation is not sufficient for reproducing the observed patterns.
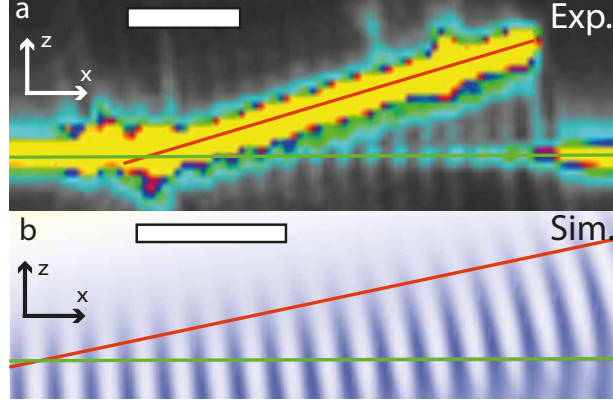
FIGURE S2. *a : Spatially resolved reflectance map in the cross sectional (X,Z) plane at 532 nm for typical sample. This experiment has been performed using scanning confocal microscopy at different focus. The intensity modulation is the signature of optical interference within the cavity. b : Interference profile of a MLG wedged cavity obtained by simulation using coherent superposition of two waves. Reflected intensity is reported in color scale, arbitrary units, white being highest intensity. This has been calculated for a wavelength of 500 nm, a numerical aperture of 0.9, reflection and transmission coefficients of 50 percent in intensity and an angle of $\alpha = 12°$. Red line corresponds to the MLG cantilever and the green line to the interface between the silicon oxide and the vacuum. Scale bars are 5 μm.*

II.   TOPOGRAPHIC CHARACTERIZATION OF THE CAVITY MEASURED BY ATOMIC FORCE MICROSCOPY

Tapping and contact mode AFM was used to characterize the MLG wedge geometry (Fig. S3). Topographic image was recorded using a non-contact AFM tip with soft spring constant (k $\sim 2N.m^{-1}$). The images were recorded across the hinge in order to obtain both suspended and lying parts of the flake. Such a micrograph is given on Fig. S3. 3D display of the data clearly shows the air wedge geometry and the hinge position. Moreover, by calculating the average cut of the topographic image on a rotated box perpendicular to the hinge, one obtains a determination of the angle between MLG and substrate ($\alpha \sim 20.4°$). After collapsing, this cantilever thickness was measured to be 72 nm (typical range is [30 ; 80nm]). Such characterization is in accordance with the angle determination obtained by reflectance (XZ) map and interfringe distance. Typical wedge angle is centered at 12 ± 2°.
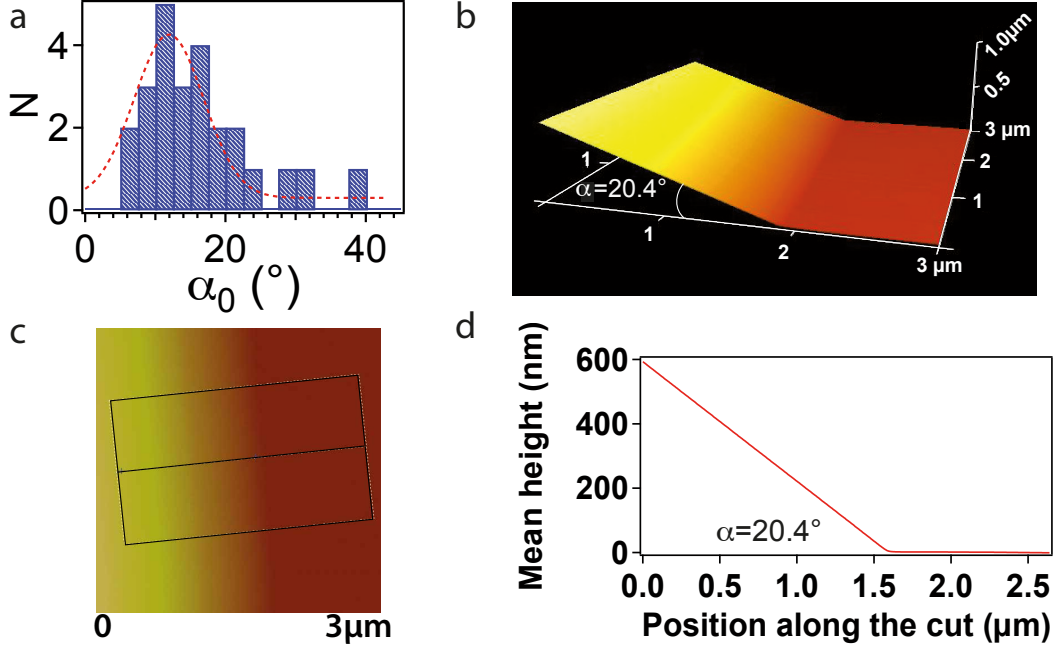
FIGURE S3. *AFM characterization of the MLG cavity.* **a** : α_0 *angle histogram. Determination of α_0 is made using AFM or confocal microscopy.* **b** : *3D topographic image recorded in contact mode showing the tilted part of the MLG.* **c** : *Same image as (b) plotted in color scale only. The rotated box defines the zone where the data have been averaged perpendicularly to the middle line.* **c** : *The averaged data provide a cut of the sample perpendicularly to the hinge direction. The angle is determined from a linear fit of this average cut.*

Moreover, it demonstrates that the MLG is stiff enough to sustain the interaction with the AFM tip without collapse.

III. GEOMETRICAL CAPACITANCE OF A WEDGE

We consider the dihedral capacitor where the two plates are : the MLG rectangular cantilever initially tilted by an angle α with respect to the substrate plane. Dielectric materials are air/vaccum ($\epsilon_r \simeq 1$) and silicon oxide ($\epsilon_r \simeq 3.9$). We model the system by two capacitors in series : C_0 corresponding to the parallel plate capacitor constituted by the silicon backgate plate and the silicon oxide surface and C_1 which is the capacitance of dihedral capacitor made by the MLG plate and the silicon oxyde surface separated by $h(\rho)$. The flake is rectangular with free parameters equal to L and W for length and width, respectively.

4

The total capacitance C_{tot} is therefore defined as follow :

$$C_{tot}^{-1} = C_0^{-1} + C_1^{-1} \tag{3}$$

Where :

$$C_0 = \frac{\epsilon_r \epsilon_0}{h_0} LW$$
$$C_1 = \iint \frac{\epsilon_0}{h(\rho)} dS = \frac{\epsilon_0 W}{sin(\alpha)} ln\left(1 + \frac{Lsin(\alpha)}{h_1}\right) \tag{4}$$

IV.   ELECTROMECHANICS OF SUSPENDED MLG CANTILEVER

A.   Electrostatic actuation of the cantilever

We modulate the cavity length $h(x,y)$ by applying a sinusoidal voltage, thus $h(x,y,t) = h(x,y)_0 + \delta h(x,y,t)$ where $h(x,y)_0$ is the local cavity length at $V = 0$. This results in an electrostatic attractive force : $\vec{F} = -\frac{1}{2}\frac{\partial C_{tot}(h)}{\partial h}V^2\vec{u_\theta} = -A[h(x,y)_0]V^2\vec{u_\theta}$. For driving frequencies $\Omega << \Omega_m$ where Ω_m is the mechanical resonant frequency, the motion of the cantilever of mass M is determined by linear response theory and $h(x,y,t)$ is then defined as the product of the mechanical susceptibility at low frequency $\chi_{mac} = M/\Omega_m^2$ and the applied force $F(t)$:

$$h(x,y,t) = \chi_{mec}F(t) = \chi_{mec}A[h(x,y)_0] \ V(t)^2 \tag{5}$$

However, when laser spot is located at 10 μm from the hinge, the deviation $\delta h(x,y,t)$ will not change significantly ($< 1\%$) the value of $A[h(x,y)_0]$ which could be approximate as a constant.

In our experiments, we manage to focus the laser beam at a location where our detection is optimum (ie. $\chi_{opt} = \partial g_{opt}/\partial h$ is maximum). Therefore, it is legitimate that I_r is locally a linear function of $h(x,y,t)$ implying that for small deflection $\delta h(x,y,t)$, the reflected light intensity (or Raman scattered light) could be written as follow :

$$I_r(t)/I_0 \sim g_{opt}(h(x,y)_0) + \frac{\partial g_{opt}}{\partial h}|_{h(x,y)_0} \ \chi_{mec}A(h(x,y)_0)V^2(t) \tag{6}$$

Eq. 6 gives the analytic ingredient to understand the festoon-like behavior presented in the main article (Fig. 2a). Note that Eq. 6 is introduced in the main text as Eq. 1. When we

5

apply a potential which is a linear function of the time, the associated change in reflected light intensity will be quadratic in time. Alternance of parabolic sections and peculiar sharp points is therefore due to the kinks of the $V(t)$ function (triangular signal).
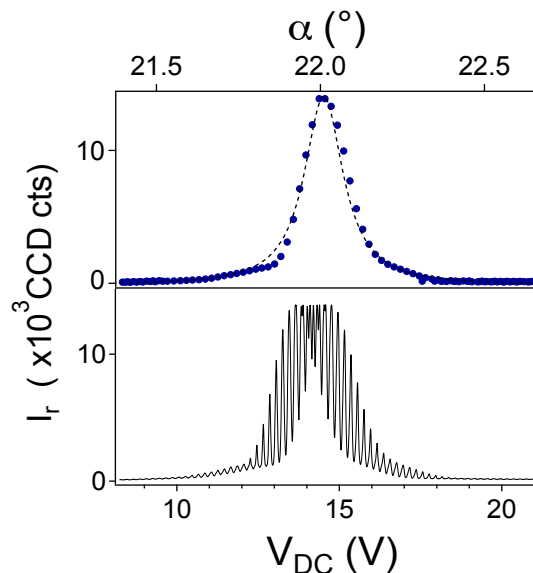
B. Quasi-static calibration of the actuation

FIGURE S4. *Bottom : reflectance intensity I_r as a function of V_{DC} under electrostatic actuation $V(t) = V_{DC} + dV(t)$ where $dV(t) \in$[-10 ; 10V]. Top : in phase envelope of I_r (●) plotted on the same V_{DC} scale. Dashed line represents the fit I_r with respect to the wedge angle (α) which allows calibration of the actuation.*

When the modulation of $\delta h = \rho.\delta\alpha$ is increased, it may become sufficiently large to explore the optical gain over an interval of the order of one interference fringe. In such a case, it is possible to calibrate the actuation. In Fig. S4, we present the reflected light versus both the wedge angle α and the DC drive voltage V_{DC}, and we show that an entire Fizeau fringe is explored. Thus by fitting the reflected intensity $I_r(t)$ with respect to α, we are able to extract the optical finesse of the cavity (~ 8) and we superimpose the evolution of I_r with V_{DC} and with α. It is then possible to calibrate precisely the variation of $h(x, y)$ induced by the voltage applied for the actuation, which equals 20 nm.V^{-2} for the sample shown in the main text.

C. Viscous damping of the mechanical resonance

The dissipation for a resonating membrane in air could be described by a simple viscous damping model[6]. The equation of motion is then modified in order to introduce a viscous force leading to a quality factor $Q_{viscous}$ defined by :

$$Q_{viscous} = \frac{2\rho t W^2 \omega}{6\pi\eta W + (3/2)\pi W^2 \sqrt{2\eta(M/RT)\omega P}}, \tag{7}$$

where $\rho = 2200$ kg.m^{-3} is the MLG density, $\eta = 1.8\ 10^{-5}$ Pa.s^{-1} is the dynamic viscosity of air, $P = 10^5$ Pa is the air pressure, $t = 180$ nm and $W = 10$ μm are respectively the MLG thickness and width for the sample described in Fig. 4c, $\omega = 7.54\ 10^6$ rad.s^{-1} is the resonant frequency of the cantilever, $T = 300$K is the ambient temperature, R is the gas constant and $M = 29$ kg.mol^{-1} is the molar mass of the gas molecule. Under such conditions, $Q_{viscous}$ equals 2.23, which is close to the experimental value of Q found in air $Q_{exp} = 2.34$.

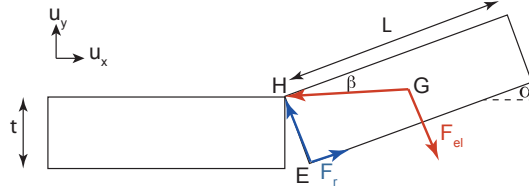## D. Mechanical model of the stress at the hinge

FIGURE S5. *Rigid hinge model for MLG cantilever. For large aspect ratio ($L/t \gg 1$), the angle $\beta = 2\tan^{-1}(t/L)$ can be neglected compared to α.*

We consider a very basic model of hinge as described by the Fig. S5. When electrostatic force $\vec{F_{el}}$ is applied on the MLG cantilever, equilibrium is reached if it exists a reaction force $\vec{F_r}$ at the hinge. In such case, torque conservation implies :

$$\vec{F_{el}} \times \vec{GH} = \vec{F_r} \times \vec{EH} \Leftrightarrow \frac{F_{el}L}{2}\begin{pmatrix} 0 \\ 0 \\ 1 \end{pmatrix} = F_r t \begin{pmatrix} 0 \\ 0 \\ 1 \end{pmatrix} \tag{8}$$

This leads to the value of an equivalent stress determined by :

$$\sigma_r = \frac{L}{W\ 2t^2}F_{el}, \tag{9}$$

7

found to be order of 50 MPa for typical device dimension and applied force (25 nN).
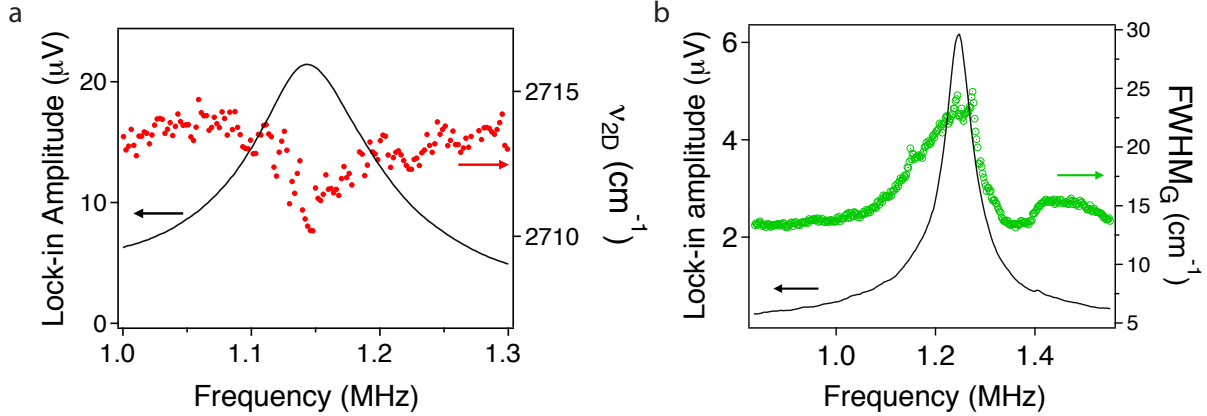
V.   RAMAN MEASUREMENTS

FIGURE S6. *Lock-in amplitude (dark line) as a function of frequency drive voltage.* **a** *: Raman 2D peak position (●) showing peak softening at mechanical resonance.* **b** *: Raman G peak FWHM (○) showing a strong increase which coincides with the MLG cantilever mechanical resonance.*

All Raman spectra have been recorded by a CCD camera with 1 kHz bandwith. In the main article, we have chosen to focus on the Raman G peak of MLG but others Raman peaks are present in the vibrational spectrum. In carbon sp^2 systems, the Raman D peak (which is not present in our case) is related to defects in the lattice. The second harmonic of the D peak, called the 2D peak, is always present and is due to scattering process involving two phonons of opposite momentum, intrinsicly obeying to the Raman selection rule ($\mathbf{q}_{tot}$ = 0). It has been shown that 2D peak is stress sensitive[7–9] and we observe a mode softening at mechanical resonance (cf. Fig. S6a)

For determination of mechanical resonance frequencies (1MHz-100MHz), Raman spectra are integrated over 1s to increase the signal over noise ratio, and this induces an experimental broadening of the Raman peak due the low bandwidth of the CCD camera (motion blur effect). The observed broadening is a superposition of that intrinsic broadening due to stress within the MLG, and the extrinsic (or experimental) broadening because of the low CCD camera bandwidth. At mechanical resonance, we present in Fig. S6b the G peak FWHM corresponding to the experiment presented in the main article (Fig. 4b).
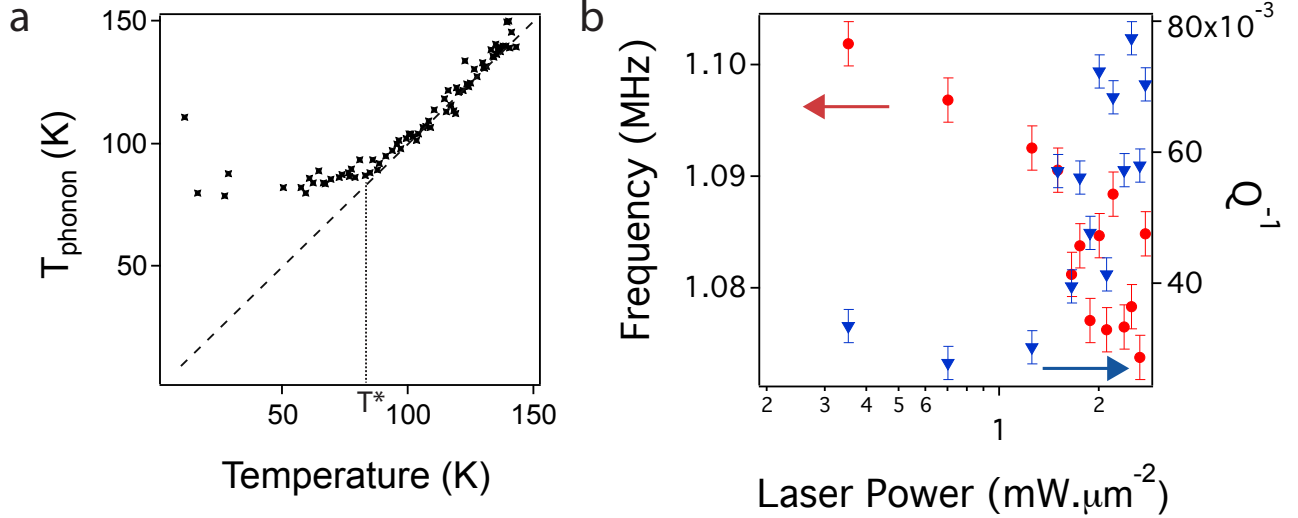
8

VI.   TEMPERATURE DEPENDENT MEASUREMENTS

FIGURE S7. *a : Temperature of the Silicon TO phonon distribution as a function of the optical cryostat temperature. Laser power is kept at 2.4 mW. Linear behavior is shown as a dashed line. b : Evolution of the f_0 MLG cantilever resonant frequency (●) and of the associated dissipation (●) as a function of the laser power. The experiment is performed under vacuum at room temperature.*

We have performed cryogenic experiments using an optical cryostat with electrical connection. As shown in the main article (Fig. 3c), the mechanical behavior of the MLG resonator drastically depends on the temperature. In parallel, we measure the Raman response of the silicon underneath as a function of the temperature. By measuring the relative occurrence of both Stokes (phonon emission) and anti-Stokes (phonon absorption) Raman scattering processes, it is possible to extract the phonon bath temperature, T_{ph} since I_{AS}/I_S is related to the Bose-Einstein distribution of the phonons :

$$\frac{I_{AS}}{I_S} \propto exp\left(-\frac{\hbar\omega_{ph}}{k_B T_{ph}}\right) \tag{10}$$

In Fig. S7b, we show that thermodynamic equilibrium is reached until the laser dissipation maintains the phonon bath temperature at a threshold at T*=70K. This important results confirms that laser probe heating is not the major dissipation mechanism at room temperature. Moreover, we present in Fig. S7b experiment performed at different laser power, indicating softening of the MLG resonator mechanical resonant frequency concomitant

9

to the increase of the dissipation. This indicates that increasing the laser power is equivalent to an increase of the local temperature. However, in all experiments presented in this paper (except Fig. S7b), laser power is kept below 1 mW.μm^{-2}, ensuring the non invasive character of the technique. Therefore, it is worth noting that these low temperature experiments demonstrate that neither mechanical nor vibrational properties of the MLG are affected by the laser at room temperature.

VII.   MOTION AND STRESS OPTICAL DETECTION OF OTHER TYPE OF NEMS.

In order to demonstrate the universality of the technique enabling optical detection of stress and motion, we present experiments on mechanical systems made of silicon. We have investigated simply clamped suspended Si and β-SiC nanowires.

A.   Actuation and Raman detection of the mechanical resonance of SOI nanowire cantilevers

Silicon nano-cantilevers are made by focused ion beam cutting of doubly clamped silicon nano-bridges presented in ref[10]. A typical micrograph of the sample is presented in Fig. S8a and this cantilever is actuated up to mechanical resonance frequency or higher harmonic by a piezo electrical actuator. When scanning the actuation frequency (see fig. S8b), the TO Raman peak softens at peculiar frequency of 11.5 MHz. It corresponds to the fundamental mechanical mode of a simply clamped beam according to finite elements simulations (see fig. S8c). The main difference between SiNWs and c-Si (bulk) arises from the confinement-induced redshift in Raman TO peak position, which equals 511.6 cm^{-1} in our case (whereas in the bulk is about 520.7 cm^{-1}). Therefore, by analogy with hydrostatic pressure studies[12–14] we obtain a relationship linking the Raman TO peak shift to the stress σ : $\Delta\nu = 5.620\ \sigma$ in gigapascal units, enabling quantitative determination of the dynamical stress amplitude at mechanical resonance, which reaches 880 MPa, according to the fig. S8b. As in carbon based resonators, we demonstrate here for silicon based NEMS, the sensitivity of Raman spectroscopy to probe and detect stress at mechanical resonances. Note that here, it was impossible to detect resonance using the elastically reflected signal. Therefore, the Raman
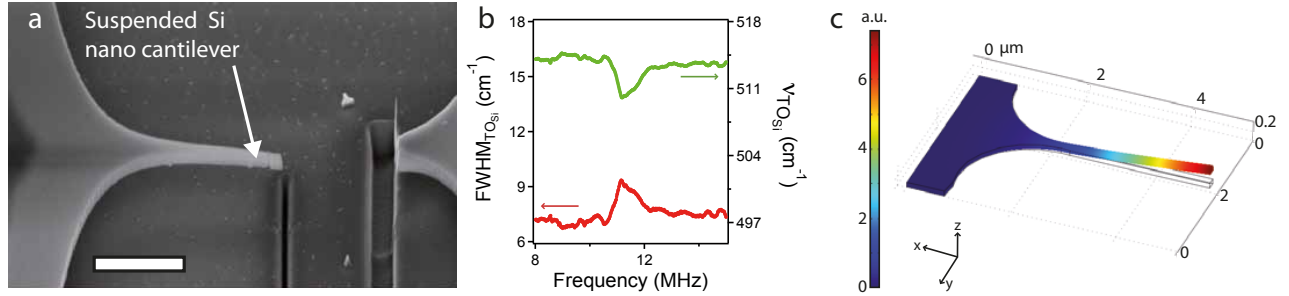
FIGURE S8. *a : SEM micrography of silicon nano-cantilever. The thickness of the beam is 100 nm. Bar scale represents 2 µm. b : Raman TO peak position (●) and FWHM (●) as a function of the actuation frequency. Experiment is performed in air, at room temperature. A significant mode softening is observed at 11.5 MHz for that silicium based NEMS. Raman peak position for each drive voltage as been rigidly shifted for presentation reasons. c : Finite elements simulation of typical geometry of silicium suspended nanowire (Young modulus is 131 GPa). The fundamental mode is found to be at 9.2 MHz under vacuum. The simulation is performed using Comsol Multiphysics software.*

detection is particularly efficient to probe mechanical resonances in such systems having all dimensions smaller than the diffraction limit, where the optical elastic response undergoes strong angular variations leading to very weak elastically scattered signals, which are difficult to discriminate from background noise.

B. Actuation and Raman detection of the mechanical resonance of SiC nanowires

The nano-mechanical resonator consists of a SiC nanowire attached to the extremity of a tungsten tip (Fig. S9a) which is rigidly fixed to a piezoelectrical actuator. Motion is recorded using a fast photodiode feeding a Vectorial Network Analyser (VNA) and thus measure the S_{21} coefficient of the system (transmittance). The resonant profile of the resonator (dark line in Fig. S9b) shows two mechanical modes slightly separated in frequency (dashed lines in Fig. S9b) which should be interpreted as loose of degeneracy of the in-plane and out-of-plane vibrations. When scanning the actuation frequency, we measure the Raman response of the SiC (β polytype, ie. diamond structure) and we focus on the TO Raman active mode, which is sensitive to strain[14] and insensitive to doping[15]. Hardening of the Raman TO peak

is seen exactly at the mechanical resonant frequency of the two modes presented here, and moreover, the Raman shift is reduced as the drive amplitude decreases. This hardening behavior is coherent with a variation of stress within the extremity of the SiC NW due to lattice compression (see for example pressure dependance of thin layers of SiC[16] or bulk material[14]). We can discriminate efficiently the resonance of the W tip from those of the SiC
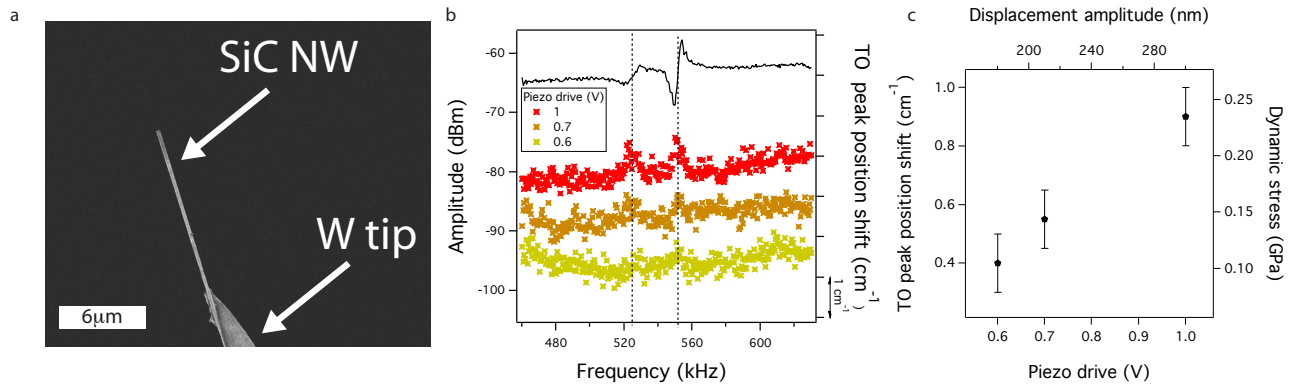

FIGURE S9. *a : SEM micrography of silicon carbide nanowire. The thickness of the beam is 100 nm. b : Amplitude of the reflected light (dark line) and Raman TO peak (779 cm^{-1}) position for different drive voltage (colors) as a function of the actuation frequency. Experiment is performed under vacuum, at room temperature. c : Raman TO peak shift at resonance as a function of the drive voltage. Drive voltage is converted to absolute displacement from deconvolution of the reflected light gaussian profile.*

nanowire as only the SiC nanowire mechanical resonance exhibits Raman shift. Therefore, as the motion amplitude reaches its maximum (*i.e.* at resonance), the dynamic stress is also maximum. Moreover, as we increase the drive energy, the dynamic stress increases as well. The latter is suggested in Fig. S9c where the Raman TO peak shift at resonance is reported *versus* the drive energy (piezo drive voltage). The linear response behavior observed here emphasis that the optomechanical coupling (*i.e.* the slope of the curve Fig. S9c) is constant for that system, within that actuation range. Converting the drive energy in absolute NW displacement allows to extract an optomechanical constant about 1.2×10^{17} Hz.m^{-1}, ranging

similarly to MLG nano-cantilevers presented in the main article.

---

[1] Blake, P. *et al.* Making graphene visible. *Applied Physics Letters*, **91**, 6 (2007).

[2] Skulason H.S., Gaskell P.E., Szkopek T. Optical reflection and transmission properties of exfoliated graphite from a graphene monolayer to several hundred graphene layers. *Nanotechnology.* **21**, 29 (2010).

[3] Hernandez-Andres J. et al. Fizeau fringes at home. *American Journal of Physics.* **70**, 7 (2002).

[4] John Rogers. Fringe shifts in multiple-beam Fizeau interferometry. *J. Opt. Soc. Am.* **72**, 5. (1982).

[5] J. Brossel. Multiple-beam localized fringes. *Proc. Phys. Soc.* **59**, 224 (1947).

[6] Hosaka, H. Itao, K. and Kuroda, S. Damping characteristics of beam-shaped micro-oscillators. *Sens. Actuators A* **49**, 87 (1995).

[7] Huang M, Yan H, Chen C, et al. Phonon softening and crystallographic orientation of strained graphene studied by Raman spectroscopy. *Proceedings of the National Academy of Sciences.* **18**, 106 (2009).

[8] Otakar, F. et al. Compression Behavior of Single-Layer Graphenes. *ACS Nano.* **4**, 6 (2010).

[9] Otakar, F. et al. Development of a universal stress sensor for graphene and carbon fibre. *Nature Comm.* **2**, 255 (2011).

[10] Heron, J.S. Fournier, T. Mingo, N. Bourgeois, O. Mesoscopic Size Effects on the Thermal Conductance of Silicon Nanowire. *Nanoletters.* **9**, 5 (2009).

[11] Anastassakis, E. Pinczuk, A. Burstein, E. Pollak, F.H. Cardona, M. Effecy of static uniaxial stress on the Raman spectrum of silicon. *Solid State Comm.* **8**, 133 (1970).

[12] Lucazeau, G. Effect of pressure and temperature on Raman spectra of solids : anharmonicity. *J. Raman Spectrosc.* **34**, 478 (2003).

[13] Bhattacharyya, S. Churochkin, D. Erasmus, R.M. Anomalous Raman features of silicon nanowires under high pressure. *Appl. Phys. Lett.* **97**, 141912 (2010).

[14] Olego, D. Cardona, M. Pressure dependence of Raman phonons of Ge and 3C-SiC. *Phys. Rev. B* **25**, 2 (1982).

[15] Yugami, H. *et al.* Characterization of the free-carrier concentrations in doped 3C-SiC crystals by Raman scattering. *Journal of Applied Physics* **61**, 354 (1987).

[16] Zhu, J. Liu, S. and Liang, J. Raman study on residual strains in thin 3C-SiC epitaxial layers grown on Si (001). *Thin Solid Films* **368**, 307-311 (2000).